Mitigation of spall fracture by evolving porosity

Edwin Chiu[a], Alan Needleman[a], Shmuel Osovski[b], Ankit Srivastava[a]

[a]*Department of Materials Science and Engineering, Texas A&M University, College Station, TX, USA*
[b]*Faculty of Mechanical Engineering, Technion - Israel Institute of Technology, Haifa, Israel*

Abstract

Ductile materials subject to impact loading conditions can undergo spall fracture when an incoming compressive stress wave reflects off interfaces and free surfaces as a tensile stress wave. Experimental observations suggest that in ductile materials, spall fracture is driven by the evolution of porosity. However, the presence of initial porosity in ductile materials also introduces plastic compressibility, which can attenuate the incoming compressive stress wave and, as a result, reduce the amplitude of the reflected tensile stress wave. This, in turn, can mitigate or delay spall fracture. In this work, we report on finite deformation finite element calculations that analyze the response of porous ductile materials subjected to impact loading conditions. Two sets of calculations are carried out, in the first set the material contains initial porosity values ranging from 0% to 5% while in the second set the material also undergoes stress-controlled porosity nucleation. Both sets of calculations are carried out for a wide range of imposed impact velocities. Our results show that porosity in ductile materials can, under certain circumstances, mitigate spall fracture by attenuating stress waves. Results correlating the effects of impact velocity, initial porosity, and porosity nucleation on spall fracture are presented and the underlying mechanisms are discussed.

Keywords: Porous Material; Plasticity; Stress Wave; Impact Loading; Spall Fracture; Finite Elements

---

1. Introduction

Materials subjected to high strain rate impact loading conditions may undergo spall fracture, due to the interaction of the incoming compressive stress wave with existing interfaces/free surfaces that result in the reflection of a tensile stress wave (Antoun et al., 2003). Experimentally, spall fracture is analyzed by subjecting one end of a specimen (referred to as the impact face) to flyer plate impact (Bourne et al., 1995; Jones et al., 2016; Chevrier and Klepaczko, 1999), high explosive charge detonation (Rybakov, 2001; Li et al., 2019), high power particle beams (Baumung et al., 1996) or electrical pulse-generated magnetic fields (Davis, 2020), and measuring the velocity profile of the corresponding opposite free end

*Corresponding author:
Email address: ankit.sri@tamu.edu (Ankit Srivastava)

(referred to as the response face), for example, by using a Velocity Interferometer System for Any Reflector (VISAR). The response face velocity profile together with knowledge of the material's initial density and bulk wave velocity can then be used to quantify the spall strength of the material given the material underwent spall fracture (Antoun et al., 2003; Kanel, 2010).

In ductile materials, spall fracture in general involves evolution of porosity (Czarnota et al., 2006; Wright and Ramesh, 2008; Me-Bar et al., 1987; Mallick et al., 2020; Thomason, 1999; Chen et al., 2006; Thissell et al., 2000; Cortes and Elices, 1995), which depends on the presence of initial porosity and/or the nucleation of porosity (Johnson, 1981; Tong and Ravichandran, 1995; Nemat-Nasser and Hori, 1987; Flanagan et al., 2022; Cui et al., 2022; Yao et al., 2018; Moore et al., 2018; Jones et al., 2018; Kraus et al., 2009). The evolution of porosity may also depend on the material microstructure (Clayton, 2005; Me-Bar et al., 1987; Remington et al., 2018; Dongare et al., 2010; Cortés, 1992; Hahn et al., 2018; Turley et al., 2018; Hashemian et al., 2008).

The presence of initial porosity renders a ductile material plastically compressible and can help attenuate the incoming compressive stress wave during impact loading conditions (Herrmann, 1969). Indeed, the attenuation of the response face velocity has been observed during impact experiments on ceramic and metallic porous foams (Jiang et al., 2021; Pramod et al., 2019; Yao et al., 2018; Bonnan et al., 1998; Jones et al., 2020), and composite materials with a layer of porous foam (Boey, 2009; Gama et al., 2001; Flanagan et al., 2022). The impact experiments on porous foam materials have also been complemented with a number of computational studies. These studies have shown that an initial high level of porosity in a material can significantly attenuate the incoming compressive stress wave and/or the response face velocity under impact loading conditions (Boey, 2009; Jiang et al., 2021; Xu et al., 2011; Erhart et al., 2005; Tang et al., 2018).

The attenuation of the response face velocity has also been observed during impact experiments on materials with rather low initial porosity levels ($\leq 5\%$) (Lovinger et al., 2020; Wang et al., 2014; Cui et al., 2022; Laurençon et al., 2020; Wang et al., 2007) that also possess adequate tensile strength required for many structural applications. Furthermore, experimental studies of Cui et al. (2022) on a titanium alloy with initial porosity levels 0.29%, 0.88% and 5.41% showed that the specimens with two lower initial porosity levels underwent spall fracture when subjected to impact velocities of 500 m/s and 620 m/s. However, the specimens with 5.41% initial porosity did not undergo spall fracture when subjected to an impact velocity of 500 m/s, although these specimens did undergo spall fracture at an impact velocity of 620 m/s. This suggests that even a low level of initial porosity in materials may be beneficial in mitigating or at least delaying spall fracture.

To explore the effect of porosity on spall fracture, we carry out finite deformation finite element calculations to analyze the response of porous ductile materials with low initial porosity levels under impact loading conditions. Specifically, two sets of calculations are carried out. In the first set, the material contains initial porosity values ranging from 0% to 5% while in the second set in addition to any initial porosity, the material undergoes stress-controlled porosity nucleation. Both sets of calculations are carried out for a wide range of imposed impact velocities. The main aims of our calculations are: (i) to investigate the effects of an initial porosity value on the attenuation of the compressive stress wave propagating through the material for a wide range of impact velocities; and (ii) to explore the extent to which the attenuation of the compressive stress wave can mitigate spall fracture due to the evolution of porosity.

2. Problem formulation and numerical method

2.1. Initial/boundary value problem

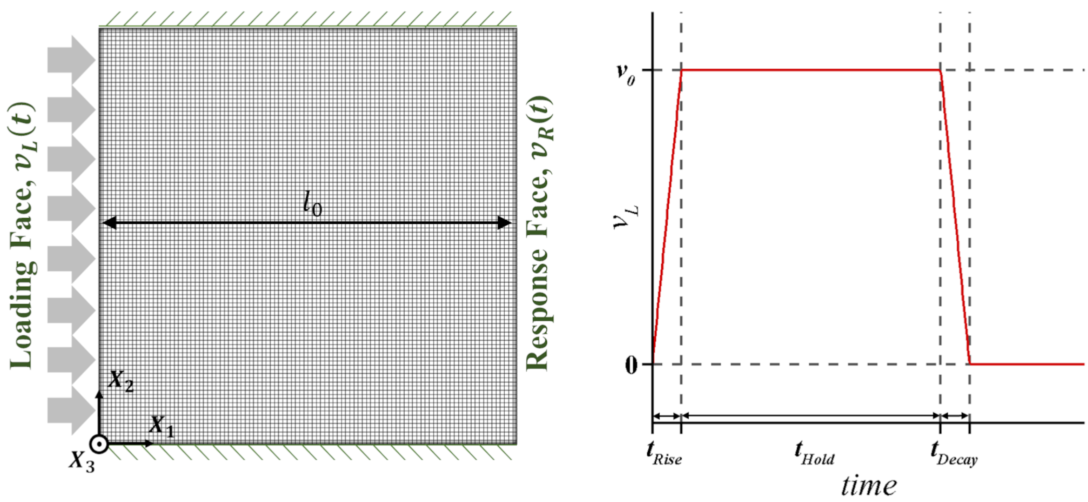

(a) (b)

Figure 1: (a) Sketch of a block subject to plane strain boundary conditions on the external faces normal to the X_2 and X_3 axes and with a velocity pulse, $v_L(t)$, prescribed on the face $X_1 = 0$ (labeled as the loading face). (b) The imposed velocity, $v_L(t)$, on the loading face with rise time, t_{Rise}, hold time, t_{Hold} and decay time, t_{Decay}.

Finite deformation finite element calculations are carried out to analyze the response of a three dimensional block subjected to uniaxial straining under an imposed one dimensional velocity pulse, as shown in Fig. 1(a). The calculations are based on a convected coordinate Lagrangian formulation of the field equations with the reference configuration taken to be the initial unstressed state. The position of a material point, relative to a fixed Cartesian frame, in the reference configuration is denoted as $\mathbf{X}$ and in the current configuration is denoted as $\boldsymbol{x}$. The displacement vector $\mathbf{u}$ and the deformation gradient $\mathbf{F}$ are written as

$$\mathbf{u} = \boldsymbol{x} - \mathbf{X} \quad , \quad \mathbf{F} = \frac{\partial \boldsymbol{x}}{\partial \mathbf{X}} \tag{1}$$

The dynamic principle of virtual work accounting for the material inertia is written as

$$\int_V \mathbf{s} : \delta \mathbf{F} dV = \int_S \mathbf{T} \cdot \delta \mathbf{u} dS - \int_V \rho \frac{\partial^2 \mathbf{u}}{\partial t^2} \cdot \delta \mathbf{u} dV \tag{2}$$

$\mathbf{s}$ is the (unsymmetric) nominal stress tensor, $\mathbf{s} = \mathbf{F}^{-1} \cdot \boldsymbol{\tau}$ with $\boldsymbol{\tau} = \det(\mathbf{F})\, \boldsymbol{\sigma}$ and $\boldsymbol{\sigma}$ being the Cauchy stress tensor, $\mathbf{T} = \mathbf{s} \cdot \mathbf{n}$ with $\mathbf{n}$ being the surface normal, ρ is the mass density in the reference configuration, t is time, and V and S are, respectively, the volume and the surface of the body in the reference configuration.

The displacement boundary conditions on $X_2 = 0, w_0$ and $X_3 = 0, h_0$, where w_0 and h_0 are the dimensions of the block along X_2 and X_3 axes, respectively, are

$$u_2(X_1, 0, X_3, t) = u_2(X_1, w_0, X_3, t) = 0 \tag{3a}$$

$$u_3(X_1, X_2, 0, t) = u_3(X_1, X_2, h_0, t) = 0 \tag{3b}$$

and the velocity boundary condition on $X_1 = 0$ is

$$\dot{u}_1(0, X_2, X_3, t) = v_L\,(t) \tag{4}$$

with $(\dot{\ })$ denoting $\partial(\ )/\partial t$.

The time variation of the imposed velocity pulse, shown in Fig. 1(b), is specified as

$$v_L(t) = \begin{cases} v_0\, t/t_{\text{rise}}, & \text{for } t \leq t_{\text{rise}} \\ v_0, & \text{for } t_{\text{rise}} < t \leq (t_{\text{rise}} + t_{\text{hold}}) \\ v_0(t_{\text{rise}} + t_{\text{hold}} + t_{\text{decay}} - t)/t_{\text{decay}}, & \text{for } (t_{\text{rise}} + t_{\text{hold}}) < t \leq (t_{\text{rise}} + t_{\text{hold}} + t_{\text{decay}}) \\ 0, & \text{for } t > (t_{\text{rise}} + t_{\text{hold}} + t_{\text{decay}}) \end{cases} \tag{5}$$

The imposed velocity pulse described in Eq. (5) is referred to as flat-top profile and is typical in flyer plate impact experiments (Dandekar and Weisgerber, 1999; Koller et al., 2005) as well as computations (Clayton, 2005) aimed at analyzing spall fracture.

2.2. *Constitutive relation*

The constitutive framework is the modified Gurson (1977) constitutive relation for a viscoplastic material matrix that has been used in a variety of previous studies, e.g., Tvergaard and Needleman (1992); Srivastava et al. (2014); Osovski et al. (2015); N'souglo et al. (2018); Liu et al. (2019). For completeness, the basic constitutive equations are listed here.

The rate of deformation tensor, $\mathbf{d} = \text{sym}(\dot{\mathbf{F}} \cdot \mathbf{F}^{-1})$, is written as the sum of an isotropic elastic (actually a hypoelastic) part, $\mathbf{d}^e$, a thermal part, $\mathbf{d}^\Theta$ and a viscoplastic part, $\mathbf{d}^p$. The elastic strains are assumed to remain small throughout the deformation history and $\mathbf{d}^e$ is given by

$$\mathbf{d}^e = \mathbf{L}^{-1} : \hat{\boldsymbol{\sigma}} \tag{6}$$

while $\mathbf{d}^\Theta$ is taken to be

$$\mathbf{d}^\Theta = \alpha \dot{\Theta} \mathbf{I} \tag{7}$$

In Eq. (6), $\hat{\boldsymbol{\sigma}}$ is the Jaumann rate of Cauchy stress and $\mathbf{L}$ is the tensor of isotropic elastic moduli characterized by the Young's modulus, E, and Poisson's ratio, ν. In Eq. (7), α is the thermal expansion coefficient and Θ is the temperature.

Adiabatic conditions are assumed so that

$$\rho c_p \dot{\Theta} = \chi \boldsymbol{\tau} : \mathbf{d}^p \tag{8}$$

where c_p is the specific heat and χ is the Taylor-Quinney factor.

The plastic part of the rate of deformation tensor, $\mathbf{d}^p$, is calculated based on the modified Gurson (1977) flow potential

$$\Phi = \frac{\sigma_e^2}{\bar{\sigma}^2} + 2q_1 f^* \cosh\left(\frac{3q_2\sigma_h}{2\bar{\sigma}}\right) - 1 - (q_1 f^*)^2 \tag{9}$$

Here, q_1 and q_2 are parameters introduced by Tvergaard (1981, 1982b), $\bar{\sigma}$ is the matrix flow strength, σ_e is the von Mises effective stress, σ_h is the hydrostatic stress, and following Tvergaard and Needleman (1984), the function f^* is given as

$$f^* = \begin{cases} f & f < f_c \\ f_c + (1/q_1 - f_c)(f - f_c)/(f_f - f_c) & f \geq f_c \end{cases} \tag{10}$$

In Eq. (10), f is the void volume fraction or simply the porosity, f_c is the critical porosity to void coalescence and f_f is the porosity at failure. The value of f at $t = 0$ denotes the initial porosity, f_0, in the material and the evolution of the porosity follows

$$\dot{f} = \dot{f}_{growth} + \dot{f}_{nucl} \tag{11}$$

where, presuming the elastic volume change to be negligible, the void growth rate or the evolution of porosity is given by the conservation of volume as

$$\dot{f}_{growth} = (1 - f)\mathbf{d}^p : \mathbf{I} \tag{12}$$

The second term in Eq. (11) models stress-controlled porosity nucleation following Chu and Needleman (1980),

$$\dot{f}_{nucl} = \begin{cases} \frac{f_N}{s_N\sqrt{2\pi}} \exp\left[-\frac{1}{2}\left(\frac{\sigma_h+\bar{\sigma}-\sigma_N}{s_N}\right)^2\right]\dot{\bar{\sigma}}\ , \text{ if } (\sigma_h + \bar{\sigma}) \geq (\sigma_h + \bar{\sigma})_{\max} \text{ and } (\dot{\sigma}_h + \dot{\bar{\sigma}}) > 0 \\ 0 \text{ otherwise} \end{cases} \tag{13}$$

where $(\ )_{\max}$ denotes the maximum over the deformation history. The Eq. (13) is based on the assumption that there is a mean strength, σ_N, for porosity nucleation and this nucleation strength is distributed in a normal fashion about the mean with standard deviation, s_N. The parameter f_N in Eq. (13) determines the maximum value of porosity that can nucleate at a material point.

The plastic part of the rate of deformation tensor, $\mathbf{d}^p$, is given as (Pan et al., 1983)

$$\mathbf{d}^p = \left[\frac{(1-f)\bar{\sigma}\dot{\bar{\varepsilon}}}{\boldsymbol{\sigma} : \frac{\partial\Phi}{\partial\boldsymbol{\sigma}}}\right]\frac{\partial\Phi}{\partial\boldsymbol{\sigma}} \tag{14}$$

with the matrix plastic strain rate, $\dot{\bar{\varepsilon}}$, taken as

$$\dot{\bar{\varepsilon}} = \dot{\varepsilon}_0 \left[\frac{\bar{\sigma}}{g(\bar{\varepsilon}, \Theta)} \right]^{1/m} \quad , \quad g(\bar{\varepsilon}, \Theta) = \sigma_0 G(\Theta) \left[1 + \bar{\varepsilon}/\varepsilon_0 \right]^N \tag{15}$$

In Eq. (15), $\dot{\varepsilon}_0$ is the reference strain rate, m is the strain-rate sensitivity exponent, σ_0 is the reference flow strength, N is the strain-hardening exponent, $\bar{\varepsilon} = \int \dot{\bar{\varepsilon}} dt$, $\varepsilon_0 = \sigma_0/E$, and $G(\Theta)$ is taken as

$$G(\Theta) = 1 + b_G \exp(-c_G[\Theta_0 - 273]) \left[\exp(-c_G[\Theta - \Theta_0]) - 1 \right] \tag{16}$$

where b_G and c_G are the parameters that control the temperature-dependence of the flow strength, and Θ_0 is the reference temperature.

2.3. Constitutive parameters

The calculations are carried out for a fixed set of values of the constitutive parameters except for the value of the initial porosity, f_0, which is taken to vary in the range $0 \leq f_0 \leq 0.05$. The fixed set of values of the other constitutive parameters considered herein do not aim at modeling a specific material but follow those used in previous analyses, e.g., Srivastava et al. (2014, 2017); N'souglo et al. (2018); Liu et al. (2019). Also, the constitutive parameters are taken to be spatially uniform so that there is no material related length scale. In the calculations, Young's modulus E is taken to be 70 GPa and Poisson's ratio ν is 0.3. In Eqs. (7) and (8), $\alpha = 1 \times 10^{-5}$ K^{-1}, $\rho = 7600$ kg/m^3, $c_p = 465$ J/(kg K), and $\chi = 0.9$. The flow potential parameters in Eq. (9) are specified as $q_1 = 1.25$ and $q_2 = 1.0$. The values of $f_c = 0.12$ and $f_f = 0.25$ are taken for Eq. (10). In Eq. (13), the mean nucleation strength is specified as $\sigma_N = 1700$ MPa, the standard deviation $s_N = 0.2\sigma_0$, and the magnitude f_N is either taken to be 0 (when the stress-controlled porosity nucleation is ignored and only the effects of the initial porosity are analyzed) or 0.04 (when the effects of both the stress-controlled porosity nucleation and initial porosity are analyzed). The material matrix hardening parameters in Eq. (15) are taken to be $\dot{\varepsilon}_0 = 10^3$ s^{-1}, $m = 0.01$, $N = 0.1$, and $\sigma_0 = 300$ MPa. The parameters controlling the temperature-dependence of the flow strength in Eq. (16) are taken to be $b_G = 0.1406$, $c_G = 0.00793$ K^{-1}, and $\Theta_0 = 293$ K.

2.4. Numerical implementation

All the calculations are carried out using an in-house three dimensional data parallel finite element code used in the previous studies, e.g., Srivastava et al. (2014); Osovski et al. (2015); Srivastava et al. (2017); N'souglo et al. (2018); Liu et al. (2019). The finite element code employs twenty node brick elements with eight point Gaussian integration for the force vector and twenty seven point Gaussian integration for the diagonal lumped mass matrix. Explicit Newmark β-method time stepping with $\beta = 0$ (Belytschko et al., 1976) is used and the constitutive updating is based on the rate tangent modulus method of Peirce et al. (1984). The material failure is implemented via the element vanishing technique proposed by Tvergaard (1982a). In this technique, when the value of the porosity, f, at an integration point reaches $0.9f_f$, the value of f is kept fixed thereafter and the material deforms with a very low flow strength.

For the initial/boundary conditions described in Section 2.1, the numerical problem is essentially one dimensional. So that the dimensions w_0 and h_0 (along X_2 and X_3 axes, respectively) of the block shown in Fig. 1(a) have no effect on the predicted response face velocity and the distribution of the stress, strain and porosity field variables. Following this, the dimensions of the block is taken to be $l_0 = 0.15$ mm and $w_0 = h_0 = 0.002$ mm, and discretized using a finite element mesh of $100 \times 1 \times 1$ elements. Limited calculations are also repeated for a block of dimensions $l_0 = w_0 = 0.15$ mm and $h_0 = 0.002$ mm discretized using a finite element mesh of $100 \times 100 \times 1$ elements for the purpose of visualization and presentation of selected results. All the calculations are carried out for the velocity pulse in Eq. (5) specified by $t_{\text{rise}} = 1$ ns, $t_{\text{hold}} = 9$ ns and $t_{\text{decay}} = 1$ ns, with the values of v_0 in the range 125 m/s $\leq v_0 \leq$ 300 m/s.

3. Uniaxial strain wave propagation

The initial/boundary value problem together with the imposed boundary conditions induce a wave that corresponds to a state of uniaxial strain. Although the formulation here is for finite deformation and allows for a complete loss of stress carrying capacity leading to spall fracture, insight into the response is obtained from a one dimensional small deformation linear elastic analysis.

With x denoting the spatial coordinate, σ the stress and v the velocity, the governing equation for one dimensional wave propagation is

$$\frac{\partial \sigma}{\partial x} = \rho \frac{\partial v}{\partial t} \tag{17}$$

and with the uniaxial strain denoted by ε, σ is given by

$$\sigma = \frac{E(1-\nu)}{(1+\nu)(1-2\nu)}\varepsilon \tag{18}$$

so that the elastic wave velocity, c, is

$$c = \sqrt{\frac{E(1-\nu)}{\rho(1+\nu)(1-2\nu)}} \tag{19}$$

where for the values of E, ν and ρ, $c = 3521$ m/s and for an impact velocity v_0 the stress carried by the wave is

$$\sigma = \rho c v_0 \tag{20}$$

Next, given a body with a geometric length that we take here to be l_0 (see, Fig. 1), we can define a characteristic time t_c and a characteristic length l_c as

$$t_c = \frac{l_0}{c} \quad , \quad l_c = l_0 \frac{c}{v_0} \tag{21}$$

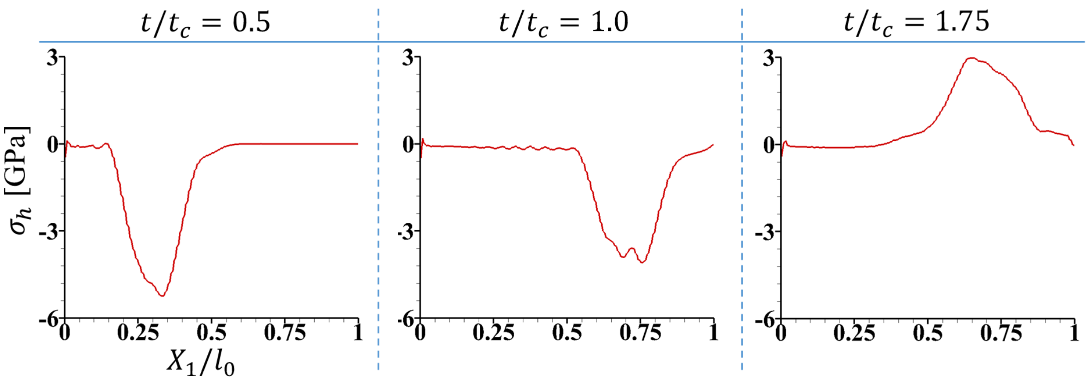

Figure 2: Variation of the hydrostatic stress, σ_h, with X_1 (the direction of imposed velocity pulse) for the boundary conditions and material parameters considered. The material is taken to be fully dense (i.e., the porosity, $f = 0$ throughout the analysis). The impact velocity is $v_0 = 250$ m/s, t is time, t_c is the characteristic time and l_0 is the dimension of the block along the X_1 axis.

Thus, although neither the constitutive relation nor the conventional governing equations contain a length scale, there is a characteristic length scale that emerges from the initial/boundary value problem formulation.

Figure 2 shows the evolution of the hydrostatic stress, σ_h, in a fully dense material (i.e., $f = 0$ throughout the analysis) subjected to an impact velocity, $v_0 = 250$ m/s, and the initial/boundary conditions described in Section 2.1. As can be seen in the figure, post-loading using the velocity pulse given in Eq. (5), a compressive stress pulse forms with a very large hydrostatic stress magnitude because the imposed strain state is nearly uniaxial strain. As this pulse propagates through the material, the magnitude of the induced hydrostatic stress decreases. At $t/t_c = 0.5$, the maximum value of the compressive hydrostatic stress is -5.3 GPa and at $t/t_c = 1.0$, the maximum value of the compressive hydrostatic stress has decreased to -4.1 GPa due to plastic dissipation. The maximum value of the compressive hydrostatic stress in the material at any give time ($t < 0.5t_c$) is found to be -6 GPa which is less than the theoretical value of -6.7 GPa estimated using the Eq. (20), also likely due to plastic dissipation. Next, as $t \to t_c$ a low amplitude elastic precursor stress wave first reaches $X_1 = l_0$ and is followed by the stronger compressive hydrostatic stress pulse traveling at a slower velocity. Finally, when the compressive hydrostatic stress pulse reaches the free surface, it is reflected as a tensile hydrostatic stress pulse. The maximum tensile hydrostatic stress in the reflected stress pulse at $t/t_c = 1.75$ is roughly 3.2 GPa.

For a material with a characteristic time, as for the viscoplastic material here, three non-dimensional ratios emerge

$$r_0 = \frac{v_0}{c} \quad , \quad r_1 = \frac{(v_0/l_0)}{\dot{\varepsilon}_0} \quad , \quad r_2 = \frac{\rho c v_0}{\sigma_0} \tag{22}$$

where r_0 provides a ratio of the impact velocity to the characteristic wave velocity, r_1 provides a ratio of the time scale associated with the loading to the material time scale and r_2 provides a ratio of the stress carried by the loading wave to the reference flow strength.

4. Numerical results

Two sets of calculations are carried out using values of the parameters specified in Section 2.3: (i) values of f_0 in the range $0 \leq f_0 \leq 0.05$ (with $f_N = 0$) to analyze the effects of initial porosity; (ii) values of f_0 in the range $0 \leq f_0 \leq 0.05$ together with stress-controlled porosity nucleation (i.e., $f_N \neq 0$) as given by Eq. (13) to analyze the effects of both initial porosity and stress-controlled porosity nucleation. Both sets of calculations are carried out for the values of the impact velocity, v_0, in the range 125 m/s $\leq v_0 \leq$ 300 m/s.

For the range of the values of v_0 considered, the non-dimensional ratios in Eq. (22) are in the range $0.036 \leq r_0 \leq 0.085$, $833.33 \leq r_1 \leq 2000$ and $11.15 \leq r_2 \leq 26.76$. These values identify the regime considered in the calculations. The value $r_0 << 1$ indicates that the impact velocity is a small fraction of the elastic wave speed. The value $r_1 >> 1$ indicates that the loading rate, v_0/l_0, is much larger than the material's characteristic strain rate, $\dot{\varepsilon}_0$. The value $r_2 >> 1$ indicates that the stress magnitude carried by the loading wave is significantly greater than the reference strength σ_0 of the material. Also, in cases where stress-controlled porosity nucleation is considered, the ratio of the stress magnitude associated with the loading wave to the nucleation stress, $\rho c v_0/\sigma_N$, is a relevant ratio and that ratio is between 1.97 and 4.72.

The stress, deformation and porosity fields obtained from the finite element calculations are, except for any round off errors, independent of X_2 and X_3 axes. When these field quantities are plotted in the $X_1 - X_2$ plane, the values shown are taken as the average of the values at $X_3 = 0$ and $X_3 = h_0$ while when such field quantities are shown as functions of X_1, the values shown are the average of those at $(X_1, w_0/2, 0)$ and $(X_1, w_0/2, h_0)$. We note that the loading condition prescribed in the calculations is an imposed velocity for all time, so that $v_L = 0$ for $t > (t_{\mathrm{rise}} + t_{\mathrm{hold}} + t_{\mathrm{decay}})$. This differs from impact loading where the impactor may eventually separate from the target material leading to a traction free surface.

4.1. Effect of initial porosity

The time evolution of the response face velocity, v_R, for materials with initial porosity values of $f_0 = 0$, 0.005, 0.015 and 0.03, subjected to impact velocities, $v_0 = 175$ m/s and 250 m/s, are shown in Figs. 3(a) and 3(b), respectively. Fig. 3 shows that for all cases the value of v_R starts to increase as $t \to t_c$ i.e., when the elastic loading wave approaches the response face. However, soon after that the value of v_R plateaus for a brief period of time before increasing and reaching a maximum value that can be greater than the value of v_0. The second increase in the value of v_R after the initial plateau is due to the trailing plastic loading wave arriving at the response face. For a fixed value of v_0, the duration of the initial plateau in the value of v_R increases with increasing f_0, while the duration of the maximum value of v_R decreases with increasing f_0. For a fixed f_0, although the duration of the velocity plateau does not strongly depend on the value of v_0, the maximum value of v_R significantly increases with increasing v_0. For $v_0 = 175$ m/s, Fig. 3(a), the maximum value of v_R is 214 m/s, 167 m/s, 78 m/s and 48 m/s, for $f_0 = 0$, 0.005, 0.015 and 0.03, respectively, while for $v_0 = 250$ m/s, Fig. 3(b), the maximum value of v_R is 330 m/s, 300 m/s, 165 m/s and 62

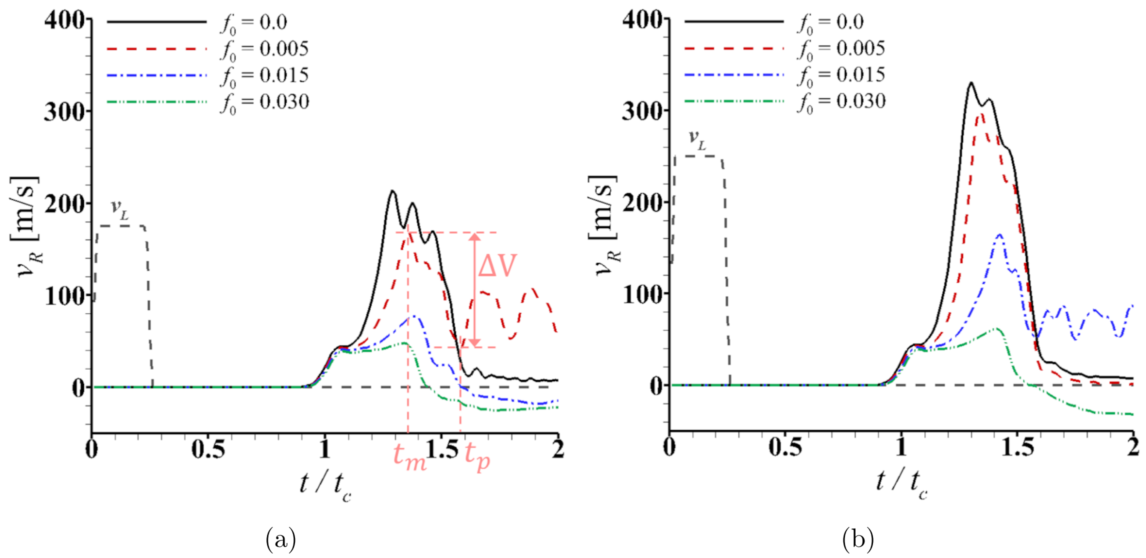

Figure 3: Effect of initial porosity, f_0, on the variation of the response face velocity, v_R, with normalized time, t/t_c. (a) Impact velocity, v_0 = 175 m/s. (b) Impact velocity, v_0 = 250 m/s. The time evolution of the imposed velocity pulse, v_L, is also plotted for reference. In (a) spall fracture occurred for $f_0 = 0.005$ and in (b) it occurred for $f_0 = 0.015$. When spall fracture occurs, the pullback velocity, ΔV, is defined as the difference between the maximum value of v_R and the subsequent first minimum value of v_R i.e., $\Delta V = v_R(t_\mathrm{m}) - v_R(t_\mathrm{p})$, as shown in (a).

m/s, for $f_0 = 0$, 0.005, 0.015 and 0.03, respectively. After reaching its maximum, the value of v_R either decays or exhibits ringing.

The ringing in the value of v_R is a consequence of spall fracture, which leads to wave reverberations between the newly formed surface and the response face. For the cases shown in Fig. 3, with $f_0 = 0.005$ spall fracture occurred for $v_0 = 175$ m/s while with $f_0 = 0.015$ spall fracture occurred for $v_0 = 250$ m/s. For calculations with sufficiently large values of f_0 the post-maximum decay of v_R can lead to negative values of v_R. This is a consequence of prescribing $v_L = 0$ for $t > t_\mathrm{rise} + t_\mathrm{hold} + t_\mathrm{decay}$.

Figure 4 shows a detailed view of the evolution of the hydrostatic stress, σ_h, leading to spall fracture for a calculation with $f_0 = 0.015$ and $v_0 = 250$ m/s. The results are shown at six values of t/t_c. As shown in Fig. 4, at $t = 0$ the material is initially stress free. A compressive stress pulse then forms and propagates through the material with gradually decreasing amplitude. The maximum compressive hydrostatic stress at $t/t_c = 0.5$ is -4.8 GPa, while at $t/t_c = 1.0$ it is -3.0 GPa. Also, as a consequence of prescribing $v_L = 0$ for $t > t_\mathrm{rise} + t_\mathrm{hold} + t_\mathrm{decay}$, the material in the wake of the propagating compressive stress pulse is not stress free. This prescribed loading condition subjects the material to a comparatively low magnitude tensile hydrostatic stress field. After reaching the response face the compressive stress pulse is reflected as a tensile stress pulse. At $t/t_c = 1.5$ the maximum tensile hydrostatic stress in the material is 1.3 GPa. At $1.5 \leq t/t_c \leq 1.75$ spall fracture occurs at a location slightly away from the response face. Following this the spalled

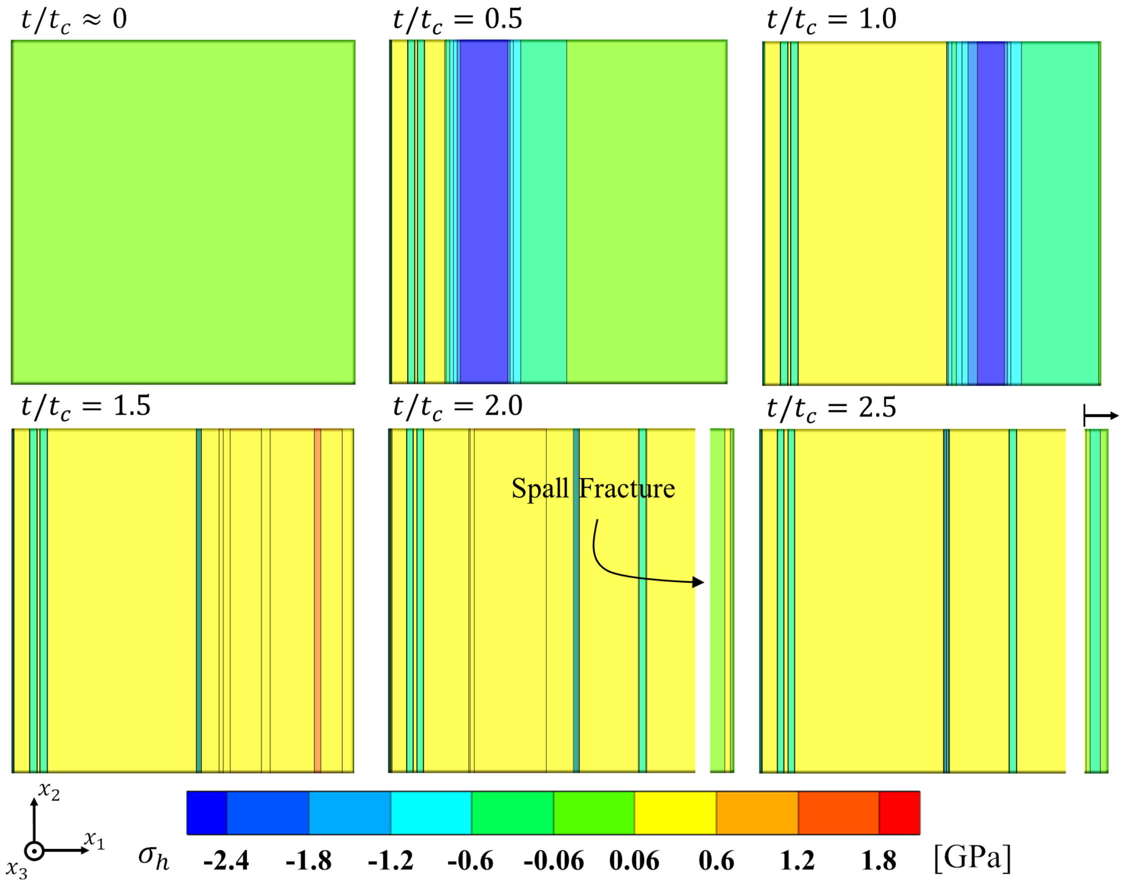

Figure 4: The spatial distribution of the hydrostatic stress, σ_h, at six values of the normalized time t/t_c for a calculation in which spall fracture occurred. The impact velocity, $v_0 = 250$ m/s and the initial porosity, $f_0 = 0.015$.

material continues to move rather freely along the positive x_1 axis as seen in the time frames $t/t_c = 2.0$ and 2.5. The stress wave reverberation within the spalled piece of material can also be seen in these time frames.

The evolution of the hydrostatic stress, σ_h, as a function of normalized position, X_1/l_0, and normalized time, t/t_c for calculations with initial porosity values of $f_0 = 0.005$, 0.015 and 0.03 with impact velocities of $v_0 = 175$ m/s and 250 m/s are shown in Fig. 5. This figure shows the formation of a compressive stress pulse that propagates through the material with decreasing magnitude. The hydrostatic stress magnitude associated with this compressive stress pulse decreases with increasing f_0, for a fixed value of v_0 while for a fixed value of f_0 the hydrostatic stress magnitude increases with increasing v_0. For example, for $v_0 = 175$ m/s and at $t/t_c = 0.5$ the compressive hydrostatic stress in the pulse is approximately -3.5 GPa, -3.2 GPa and -2.4 GPa for $f_0 = 0.005$, 0.015 and 0.03, respectively, while at $t/t_c = 1.0$ it is approximately -2.4 GPa, -1.3 GPa and -0.5 GPa for $f_0 = 0.005$, 0.015 and 0.03, respectively. Similarly, for $v_0 = 250$ m/s and at $t/t_c = 0.5$ the magnitude of the hydrostatic

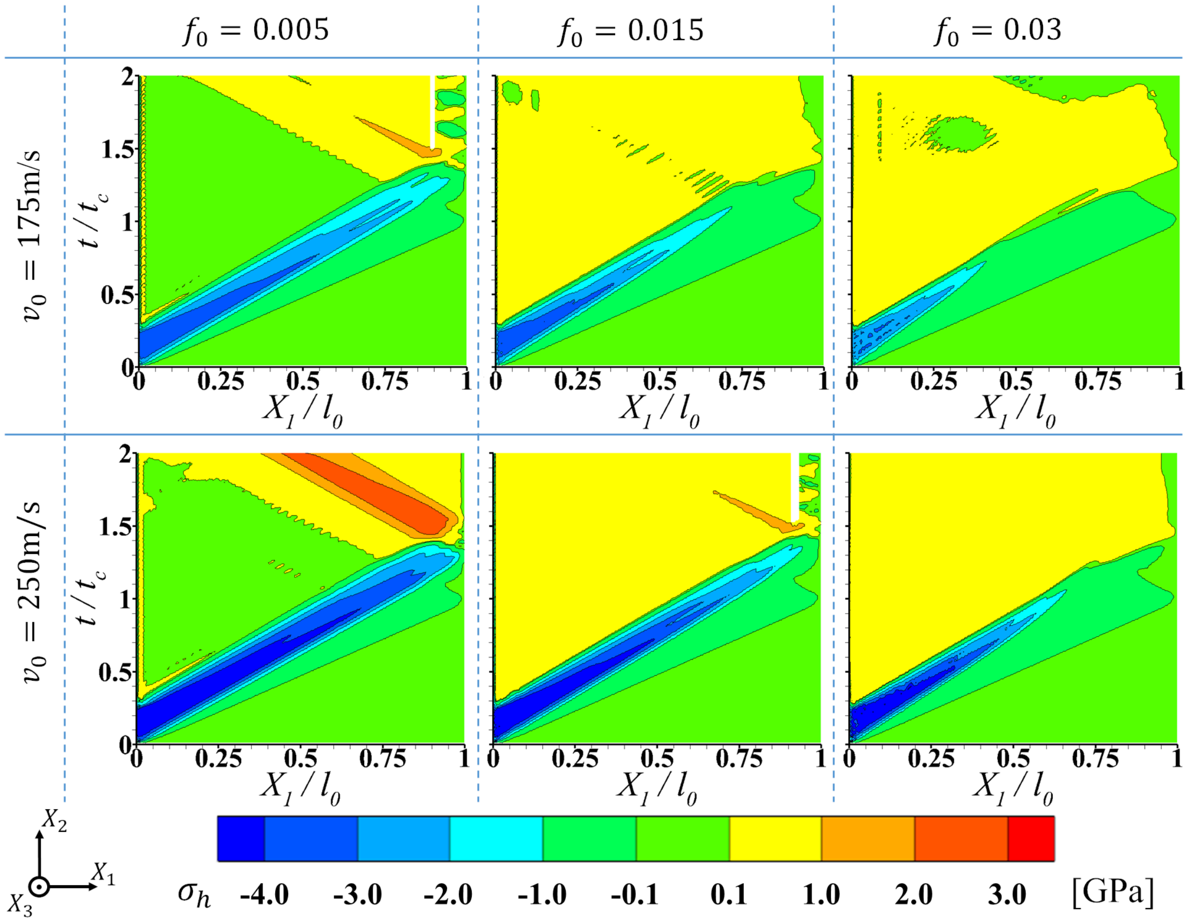

Figure 5: The variation of the hydrostatic stress, σ_h, with normalized position, X_1/l_0, and time, t/t_c, for $f_0 = 0.005, 0.015$ and 0.03, and $v_0 = 175$ m/s and 250 m/s. The white regions in the plots for $v_0 = 175$ m/s, $f_0 = 0.005$ and for $v_0 = 250$ m/s, $f_0 = 0.015$ mark the spall fracture.

stress associated with the stress pulse is approximately -5.1 GPa, -4.8 GPa and -4.2 GPa for $f_0 = 0.005$, 0.015 and 0.03, respectively, while at $t/t_c = 1.0$ it is approximately -3.8 GPa, -3.0 GPa and -1.3 GPa for $f_0 = 0.005$, 0.015 and 0.03, respectively. Furthermore, the rate of decrease of the hydrostatic stress magnitude associated with this compressive stress pulse also increases with increasing f_0. For example, for $v_0 = 250$ m/s the magnitude of the hydrostatic stress at $X_1/l_0 = 0.5$ (which occurs at $t/t_c \approx 0.64$, 0.69 and 0.76) has decreased by approximately 83%, 68% and 46% for $f_0 = 0.005$, 0.015 and 0.03, respectively.

From the contour plots in Fig. 5 the time it takes for a fixed value of the compressive hydrostatic stress to propagate between two positions in the material can be tracked, from which the plastic loading wave velocity can be estimated. Using the time it takes for a value of $\sigma_h = -2$ GPa to first reach $X_1/l_0 = 0.05$ and 0.25, the plastic loading wave velocity for $v_0 = 175$ m/s is estimated to be $0.76c$, $0.7c$ and $0.6c$ for $f_0 = 0.005$, 0.015 and 0.03, respectively, and for $v_0 = 250$ m/s it is estimated to be $0.78c$, $0.75c$ and $0.68c$ for $f_0 = 0.005$, 0.015 and 0.03, respectively. This shows that the velocity of the front of the plastic loading wave decreases significantly with increasing f_0 and increases with increasing v_0. The contour plots in Fig. 5 also show the evolution of the comparatively low magnitude tensile hydrostatic stress near the impact face that develops in the wake of the compressive stress pulse. This tensile hydrostatic stress is a consequence of the imposed velocity boundary condition as noted previously. The level of this tensile hydrostatic stress increases with increasing porosity f_0 because of the associated increase in plastic deformation. Also, the magnitude of this tensile hydrostatic stress increases with increasing v_0 due to the increase in the overall stress magnitude in the material.

As for the compressive hydrostatic stress, the magnitude of the reflected tensile hydrostatic stress for a fixed value of v_0 also decreases with increasing initial porosity f_0, and for a fixed value of f_0 increases with increasing velocity v_0. For example, with $v_0 = 175$ m/s the maximum value of the reflected tensile hydrostatic stress is found to be about 1.4 GPa and 0.67 GPa for $f_0 = 0.005$ and $f_0 = 0.03$, respectively, while for $v_0 = 250$ m/s it is approximately 2.9 GPa and 0.74 GPa, for $f_0 = 0.005$ and $f_0 = 0.03$, respectively. The location of the maximum value of the reflected tensile hydrostatic stress is always slightly away from the response face, as can be seen for $v_0 = 250$ m/s and $f_0 = 0.005$ in Fig. 5 for which the maximum value is at $X_1/l_0 \approx 0.88$. This is due to the destructive interference close to the response face between the incoming compressive hydrostatic stress pulse and the reflected tensile hydrostatic stress pulse. The reflected tensile hydrostatic stress can lead to spall fracture. However, the propensity for spall fracture will depend on the magnitude of the reflected tensile hydrostatic stress and the current level of porosity. Both of which depend on the values of v_0 and f_0. For the cases shown in Fig. 5, spall fracture occurs for $v_0 = 175$ m/s and $f_0 = 0.005$ at $t/t_c \approx 1.5$ and $X_1/l_0 \approx 0.9$, and for $v_0 = 250$ m/s and $f_0 = 0.015$ at $t/t_c \approx 1.52$ and $X_1/l_0 \approx 0.92$. In Fig. 5, the white regions in the contour plot mark the spall fracture.

Figure 6 shows the evolution of porosity, f, as a function X_1/l_0 and t/t_c for calculations with $f_0 = 0.005$, 0.015 and 0.03, and with $v_0 = 175$ m/s and 250 m/s. Although a value of 0.12 is taken for the critical porosity, f_c, in Eq. (10), for all calculations shown, the maximum value of f in the contour plots in Fig. 6 is taken to be 0.04 for clarity of visualization. As shown in the figure and as expected, the value of f at a material point decreases due to the compressive hydrostatic stress associated with the initial pulse. At the early stages i.e., closer to the loading face and loading time, the decrease in the value of f, regardless of the values of v_0 and f_0 is large. In all cases, the values of f at these positions and times have decreased below 10^{-4} (but remain positive). Nevertheless, since for a fixed value of v_0 the rate of decrease of the magnitude of the compressive hydrostatic stress increases with increasing f_0, the distance, X_1/l_0, over which the value of f decreases significantly also decreases with increasing f_0. While for a fixed value of f_0 the distance, X_1/l_0, over which the value of f decreases significantly increases with increasing impact velocity v_0. For example, for $v_0 = 175$ m/s at $t/t_c \approx 1.3$ i.e., just before the compressive hydrostatic stress reflects as a tensile hydrostatic stress, $f < 10^{-3}$ for $X_1/l_0 < 0.87$, $X_1/l_0 < 0.58$ and $X_1/l_0 < 0.34$ for the cases with $f_0 = 0.005$, $f_0 = 0.015$ and $f_0 = 0.03$, respectively. Similarly, for $v_0 = 250$ m/s, $f < 10^{-3}$ for $X_1/l_0 < 0.98$, $X_1/l_0 < 0.89$ and $X_1/l_0 < 0.6$ for the case with $f_0 = 0.005$,

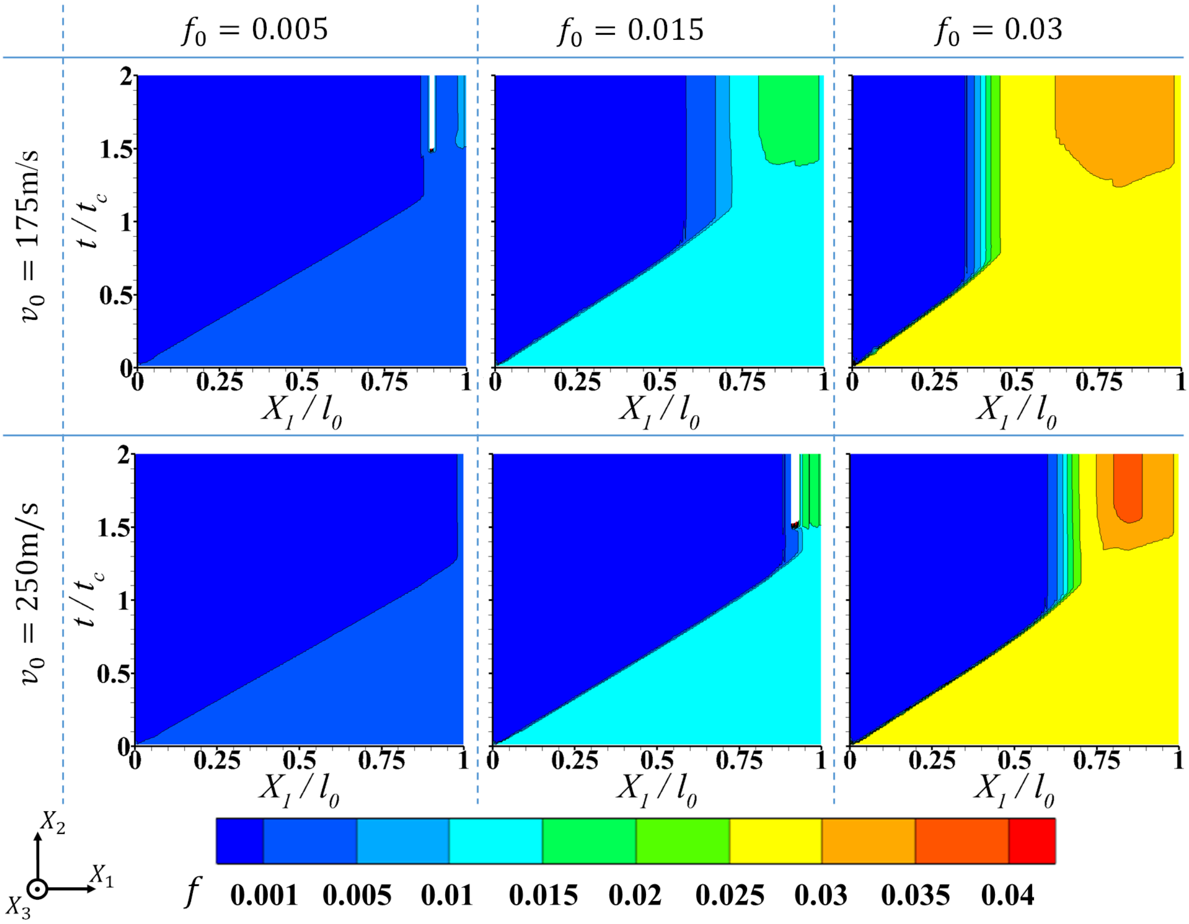

Figure 6: The variation of porosity, f, with normalized position, X_1/l_0, and time, t/t_c, for $f_0 = 0.005, 0.015$ and 0.03, and $v_0 = 175$ m/s and 250 m/s. The white regions in the plots for $v_0 = 175$ m/s, $f_0 = 0.005$ and for $v_0 = 250$ m/s, $f_0 = 0.015$ mark the spall fracture.

$f_0 = 0.015$ and $f_0 = 0.03$, respectively.

Due to the tensile hydrostatic stress in the reflected pulse, the porosity f increases. However, the rate of increase of the value of f, depends on both the current value of f and on the magnitude of the tensile hydrostatic stress in the reflected stress pulse. Both of these in turn depend on the values of initial porosity f_0 and impact velocity v_0. For example, for $f_0 = 0.005$ and $v_0 = 175$ m/s, the current value of f near the response face and the magnitude of the tensile stress in the reflected pulse are both sufficiently large for spall fracture to occur. While for $f_0 = 0.005$ and $v_0 = 250$ m/s, even though the magnitude of the tensile hydrostatic stress is sufficiently high, the current value of f near the response face is so low that spall fracture does not occur. On the other hand, for $f_0 = 0.03$ even though the current value of f is relatively large, the magnitude of the tensile hydrostatic stress in the reflected stress pulse is so low that spall fracture does not occur for both values of impact velocity.

4.2. Effect of stress-controlled porosity nucleation

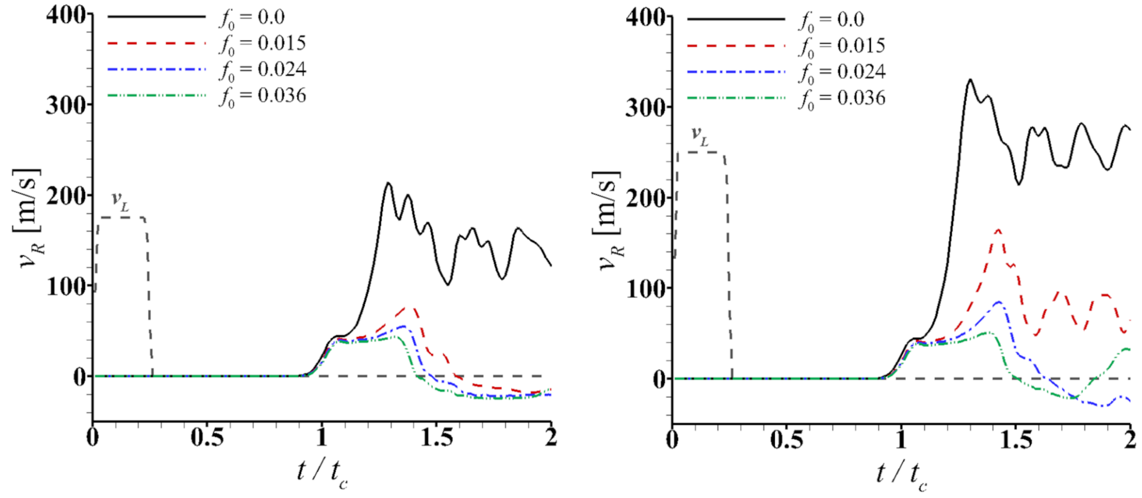

(a) (b)

Figure 7: The response face velocity, v_R versus normalized time, t/t_c, for calculations with stress-controlled porosity nucleation and for various values of initial porosity, f_0. (a) Impact velocity, v_0 = 175 m/s. (b) Impact velocity, v_0 = 250 m/s. The time evolution of the imposed velocity pulse, v_L, is also plotted for reference. In (a) spall fracture occurred for $f_0 = 0$ and in (b) it occurred for both $f_0 = 0$ and $f_0 = 0.015$.

Figure 7 shows the time evolution of the response face velocity, v_R, for initial porosity values of f_0 = 0, 0.015, 0.024 and 0.036, subjected to impact velocities of v_0 = 175 m/s and 250 m/s for calculations with stress-controlled porosity nucleation, Eq. (13). The time evolution of v_R until v_R reaches its maximum value in Fig. 7 follows the same trend as in Fig. 3 where porosity nucleation is not included. However, the time evolution of v_R after v_R reaches the maximum value can differ between Figs. 3 and 7 depending on the values of f_0 and v_0. For example, with stress-controlled porosity nucleation for both v_0 = 175 m/s and 250 m/s, the value of v_R exhibits ringing due to spall fracture even for $f_0 = 0$. Nevertheless, for several cases the time evolution of v_R after v_R reaches the maximum value is also the same in Figs. 3 and 7. For example, for f_0 = 0.015 and v_0 = 175 m/s or 250 m/s, the time evolution of v_R is nearly the same with or without stress-controlled porosity nucleation. Fig. 7(b) includes a case with f_0 = 0.036 and v_0 = 250 m/s, for which the value of v_R post-maximum first decays and then tends to increase. This is attributed to the imposed loading condition leading to damage at the impact face as explained later.

The evolution of the hydrostatic stress, σ_h, as a function of normalized position, X_1/l_0, and normalized time, t/t_c for calculations with stress-controlled porosity nucleation and initial porosity levels, f_0 = 0, 0.015 and 0.036, and impact velocities, v_0 = 175 m/s and 250 m/s, are shown in Fig. 8. Many features of the results shown here are also similar to those shown in Fig. 5 where only the effects of the initial porosity in the material is

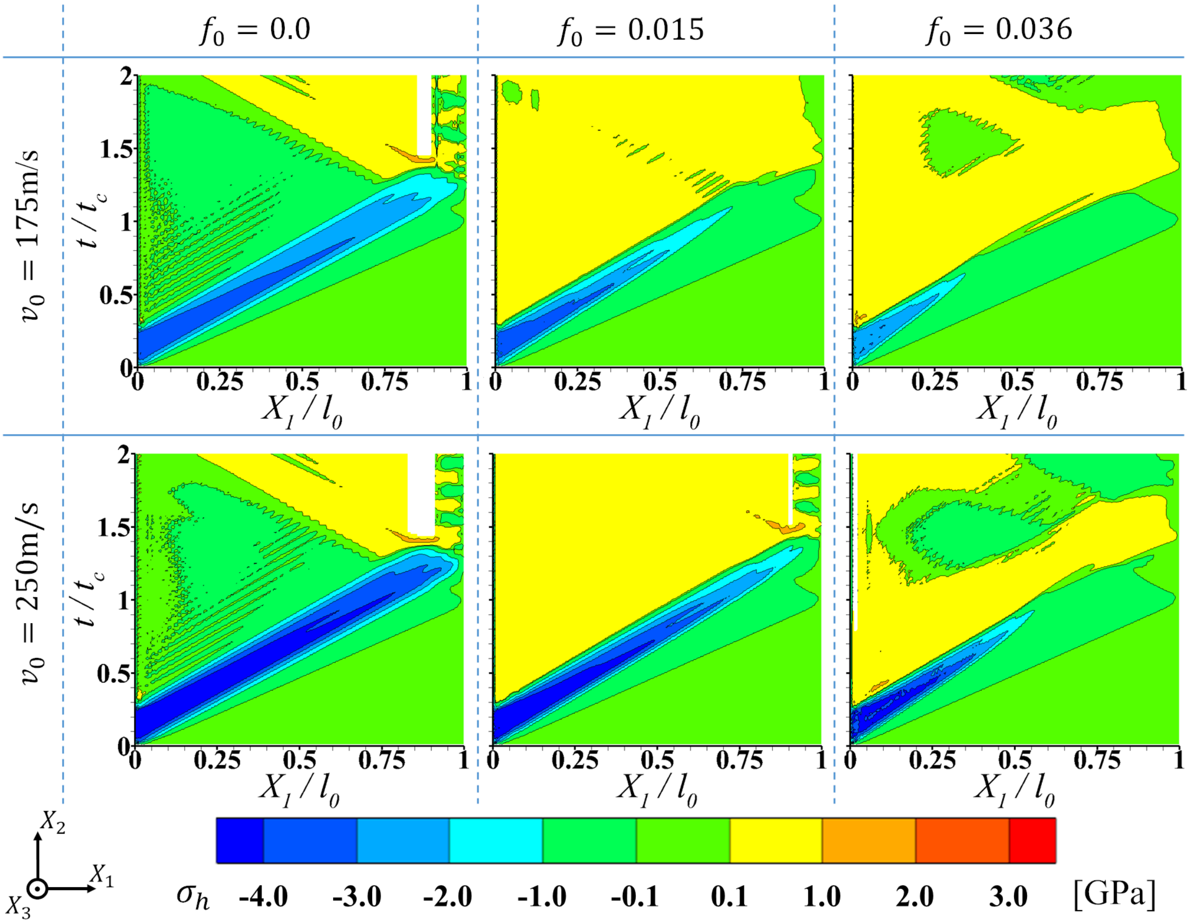

Figure 8: The variation of the hydrostatic stress, σ_h, with normalized position, X_1/l_0, and time, t/t_c, for calculations with stress-controlled porosity nucleation and with $f_0 = 0, 0.015$ and 0.036, and $v_0 = 175$ m/s and 250 m/s. The white regions in the plots for $v_0 = 175$ m/s, $f_0 = 0$, for $v_0 = 250$ m/s, $f_0 = 0$ and for $v_0 = 250$ m/s, $f_0 = 0.015$ mark the spall fracture.

modeled. However, because in these cases voids can nucleate following the stress-controlled nucleation criterion, Eq. (13), spall fracture occurs as long as the magnitude of the tensile hydrostatic stress in the reflected pulse is sufficiently high. Thus, with stress-controlled porosity nucleation, spall fracture can occur even with no initial porosity ($f_0 = 0$) as shown in Fig. 8. The magnitude of the tensile hydrostatic stress in the reflected pulse for a fixed value of impact velocity v_0 decreases with increasing f_0, and for a fixed value of f_0 increases with increasing v_0. Thus, for $v_0 = 175$ m/s spall fracture does not occur for sufficiently large values of f_0, for example, for $f_0 = 0.015$ and 0.036 in Fig. 8 but for a fixed value of f_0 spall can occur for a sufficiently large value of v_0 as is the case for $f_0 = 0.015$ with $v_0 = 250$ m/s.

Figure 9 shows the evolution of porosity, f, as a function X_1/l_0 and t/t_c for calculations with stress-controlled porosity nucleation and with initial porosity values $f_0 = 0$, 0.015 and 0.036, and impact velocities $v_0 = 175$ m/s and 250 m/s.The evolution of porosity before the

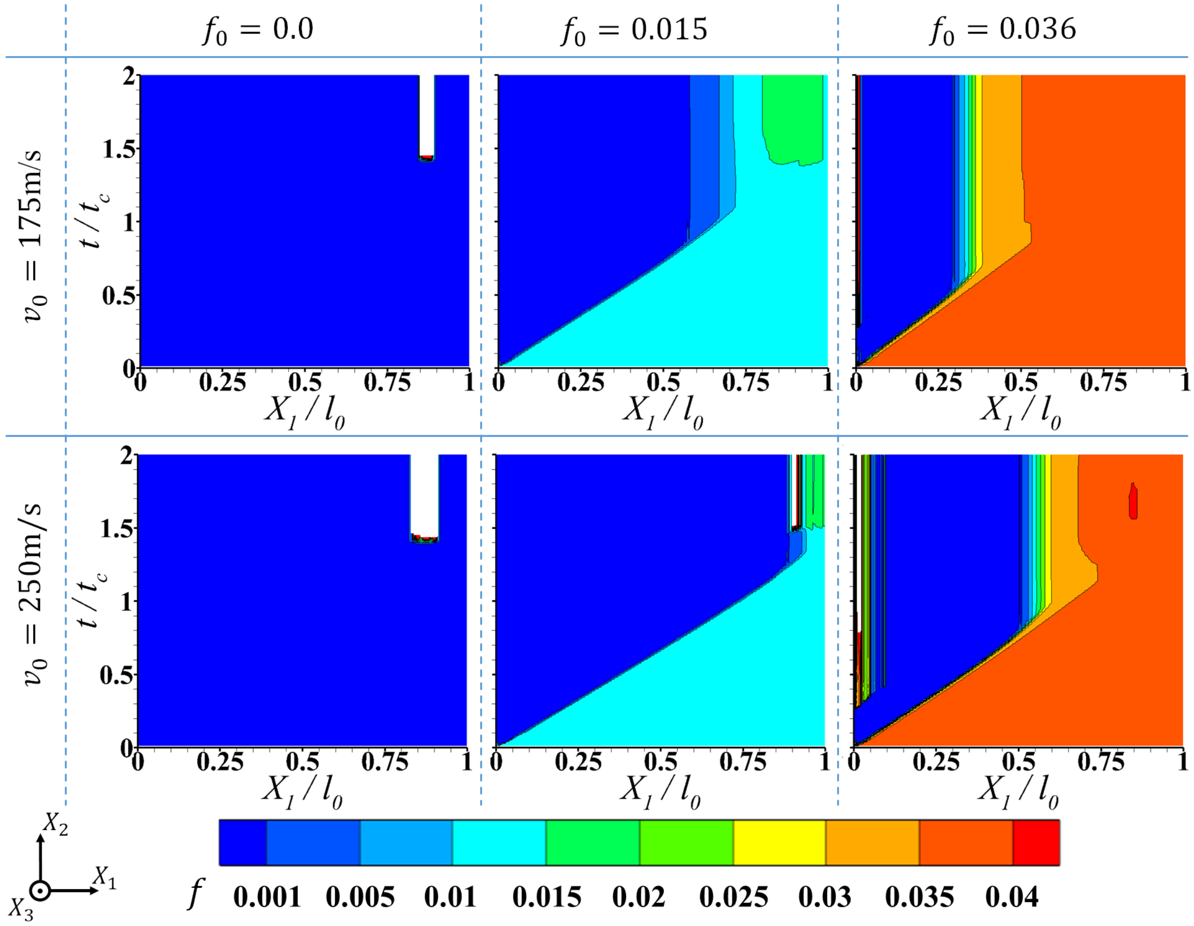

Figure 9: The variation of porosity, f, with normalized position, X_1/l_0, and time, t/t_c, for calculations with stress-controlled porosity nucleation and with $f_0 = 0, 0.015$ and 0.036, and $v_0 = 175$ m/s and 250 m/s. The white regions in the plots for $v_0 = 175$ m/s, $f_0 = 0$, for $v_0 = 250$ m/s, $f_0 = 0$ and for $v_0 = 250$ m/s, $f_0 = 0.015$ mark the spall fracture.

compressive stress pulse reflects as a tensile stress pulse is the same as for the cases without stress-controlled porosity nucleation. However, as shown in the figure with stress-controlled porosity nucleation, the reflected tensile stress pulse can lead to nucleation of voids that can grow and cause spall fracture even for the cases with $f_0 = 0$. Also, because the magnitude of the tensile stress in the reflected pulse increases with increasing impact velocity v_0, the width over which stress-controlled porosity nucleation occurs also increases with increasing v_0. For all cases with $f_0 > 0$, the magnitude of the tensile stress in the reflected pulse also depends on the value of f_0. So that for $v_0 = 175$ m/s, and $f_0 = 0.015$ and 0.036 even though the current value of $f > 0$, the stress magnitude in the reflected tensile pulse is not sufficient to cause spall fracture due to porosity nucleation and growth. While for $v_0 = 250$ m/s and $f_0 = 0.015$ both the value of f near the response face and the stress magnitude associated with the reflected pulse are sufficiently large for spall fracture to occur.

The tensile hydrostatic stress magnitude near the impact face that develops due to the imposed loading conditions can also lead to the nucleation and growth of porosity. Because the magnitude of the tensile hydrostatic stress increases with increasing values of v_0 and f_0, for sufficiently large values of v_0 and f_0, this can lead to impact face damage as shown in Fig. 9 for the case with $v_0 = 250$ m/s and $f_0 = 0.036$. This impact face damage is the reason that values of v_R may increase following the post-maxima decay for cases with sufficiently large values of v_0 and f_0 as in Fig. 7(b).

4.3. Spall fracture and spall strength

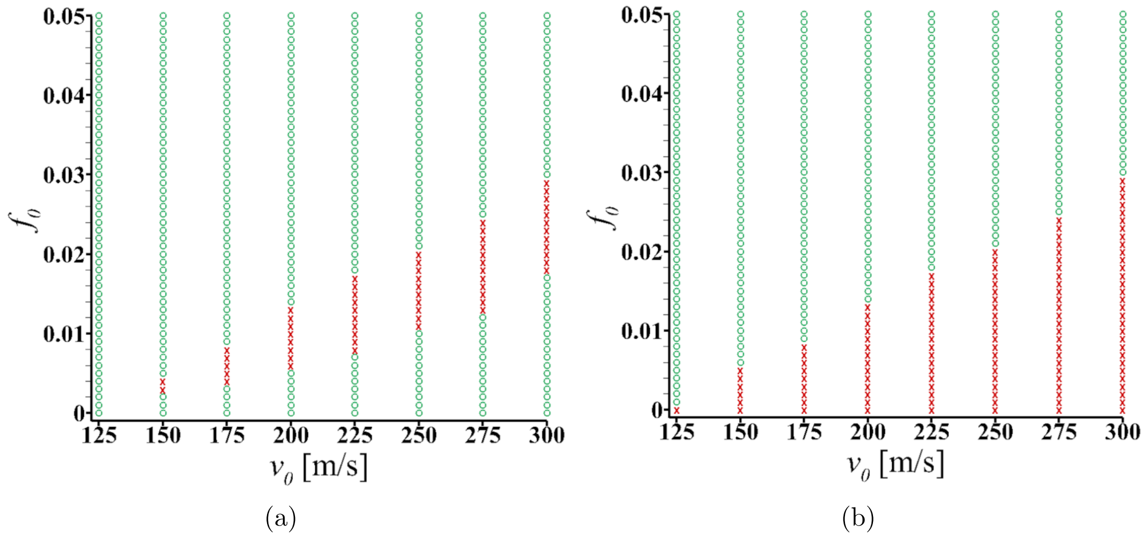

Figure 10: The dependence of spall fracture (marked by '×' symbols) or no spall fracture (marked by 'o' symbols) on the initial porosity, f_0, and the impact velocity, v_0. (a) For calculations with only an initial porosity. (b) For calculations with an initial porosity together with stress-controlled porosity nucleation.

The dependence of spall fracture on initial porosity, f_0, and impact velocity, v_0, is shown in Fig. 10. Fig. 10(a) shows results for calculations with only initial porosity and Fig. 10(b) shows results for initial porosity together with stress-controlled porosity nucleation. Calculations for which spall fracture occurred are marked with a red '×' and calculations for which spall fracture did not occur are marked with a green 'o'.

Figure 10(a) shows that with only initial porosity, spall fracture does not occur for $v_0 = 125$ m/s for the range of values of f_0 considered. For $v_0 \geq 150$ m/s there is a minimum value of f_0 needed to trigger spall fracture and this minimum value of f_0 increases approximately linearly with increasing v_0. For $v_0 \geq 150$ m/s there is also a maximum value of f_0 above which spall fracture does not occur. This maximum value of f_0 also increases roughly linearly with increasing v_0. The rate of increase of the maximum value of f_0 with v_0 above which spall does not occur is greater than the rate of increase of the minimum value of f_0 with v_0 below which spall does not occur. Hence, the range of the values of f_0 over which spall does occur increases with increasing v_0.

In Fig. 10(b), for calculations with both initial porosity and stress-controlled porosity nucleation, there is no minimum value of f_0 below which spall does not occur. Nevertheless, there is a maximum value of f_0 above which spall fracture does not occur, which also increases nearly linearly with increasing v_0. The maximum value of f_0 above which spall does not occur for a fixed value of v_0 is approximately the same as for the calculations without stress-controlled porosity nucleation.

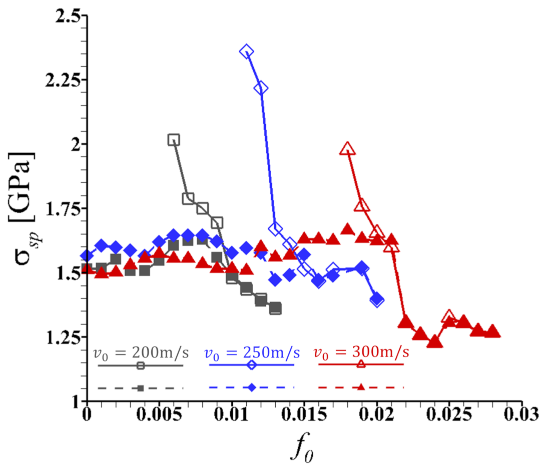

Figure 11: The variation of the spall strength, σ_{sp}, with initial porosity, f_0, for three values of the impact velocity, v_0, for calculation in which spall fracture occurred. The solid lines and open symbols correspond to calculations with only an initial porosity. The dashed lines and closed symbols correspond to calculations with an initial porosity together with stress-controlled porosity nucleation.

Figure 11 shows the variation of the spall strength, σ_{sp}, with f_0 for three values of v_0 for both the calculations with only initial porosity and those with initial porosity together with stress-controlled porosity nucleation. The value of σ_{sp} is given by

$$\sigma_{sp} = \frac{1}{2}\rho c \Delta v \tag{23}$$

where ρ is the initial density of the material, c is the elastic wave velocity given in Eq. (19) and ΔV is the pullback velocity defined in Fig. 3(a).

For a fixed value of v_0, the value of σ_{sp} with only initial porosity initially decreases rapidly with increasing f_0 and then tends to saturate. For a fixed value of f_0, the value of σ_{sp} increases with increasing v_0. The magnitude of the increase in σ_{sp} with increasing v_0 depends on the value of f_0 and increases with decreasing f_0.

When both initial porosity and stress-controlled porosity nucleation are considered, the value of σ_{sp} remains nearly constant irrespective of f_0 and v_0 until f_0 exceeds a certain threshold value that increases with increasing v_0. For smaller values of f_0, i.e., below the threshold value of f_0, the values of σ_{sp} with stress-controlled porosity nucleation are smaller than the corresponding values without stress-controlled porosity nucleation. However, for

f_0 greater than the v_0 dependent threshold value of f_0, σ_{sp} decreases with increasing f_0 and is identical to the calculations without stress-controlled porosity nucleation.

5. Discussion

We have carried out finite deformation finite element calculations to analyze the response of porous ductile materials under impact loading for values of initial porosity, f_0, in the range $0 \leq f_0 \leq 0.05$ and for values of impact velocity, v_0, in the range 125 m/s $\leq v_0 \leq$ 300 m/s.

Our calculations capture the plastic deformation and porosity compaction due to the propagation of the compressive stress pulse. These in turn lead to a decrease in the stress magnitude in the pulse. The results show that an increase in the initial porosity level results in an even greater decrease in the stress magnitude, but subsequently it also decreases the extent of compaction of the porous material. While an increase in impact velocity (for a fixed initial porosity value) leads to an increase in both the magnitude of the compressive stress and the extent of compaction of the porous material.

Because our focus is on analyzing the effects of porosity-induced plastic compressibility on the response of porous ductile materials subjected to impact loading, we assumed that the elastic response of the material is linear. However, when a material is subjected to very high impact velocities and/or pressures, the assumption of linear elasticity may no longer be appropriate, and the bulk modulus of the material may vary with pressure. Nevertheless, experiments suggest that nonlinear elasticity only becomes significant at impact velocities greater than several km/s and pressures greater than tens of GPa (Walsh and Christian, 1955; Holmes et al., 1989; Trunin et al., 1989; Reinhart et al., 2001). Meeting either of these conditions requires parameter values an order of magnitude greater than those used in our calculations.

In calculations where growth of pre-existing porosity is the only damage mechanism, the propensity for spall fracture depends on the stress magnitude in the reflected pulse and the current level of porosity in the material. Thus, for these materials there is a minimum level of initial porosity below which the current level of the porosity is too small for spall fracture to occur. There is also a maximum level of initial porosity above which the magnitude of the reflected tensile stress is too small for spall fracture to occur. Both the minimum and maximum critical levels of the initial porosity increase with increasing impact velocity, with the increase in the maximum critical porosity level being greater than the increase in the minimum critical porosity level. This results in an increase in the range of values of initial porosity over which spall fracture occurs with increasing impact velocity.

When stress-controlled porosity nucleation is included in the calculations, spall fracture can occur due to stress-controlled porosity nucleation, even in the absence of initial porosity, as long as the tensile stress magnitude is large enough to nucleate sufficient porosity. Hence, for the values of the parameters characterizing stress-controlled porosity nucleation considered in this work, there is no minimum initial porosity level below which spall fracture does not occur. However, there is a maximum initial porosity level above which spall fracture does not occur, and this maximum porosity level increases with increasing impact velocity. Additionally, for the considered parameter values, these maximum initial porosity values are almost the same for calculations, both with and without stress-controlled porosity nucleation. Although not presented here, we also carried out limited parametric analyses to examine the effects of the two parameters characterizing stress-controlled porosity nucleation, namely f_N and σ_N. Among the two parameters, f_N and σ_N, σ_N had a more significant effect on the propensity of spall fracture to occur because the stress level must reach σ_N for porosity nucleation. The results of these parametric analyses showed that increasing σ_N results in a minimum value of the initial porosity (for a fixed value of the imposed impact velocity) below which spall fracture does not occur, as in the scenario without stress-controlled porosity nucleation. Also, decreasing σ_N results in an increase in the value of the maximum initial porosity level above which spall fracture does not occur.

If spall fracture results from the evolution of pre-existing porosity, the spall strength decreases with increasing initial porosity, and it increases with increasing impact velocity. However, when spall fracture is driven by stress-controlled porosity nucleation, over the range investigated, the spall strength is not very sensitive to the value of initial porosity or to the value of impact velocity.

Although the values of the constitutive parameters considered in this work do not correspond to a specific material but represent a generic porous ductile material, several features of our results are consistent with the limited experimental studies of spall fracture in porous ductile materials. For example, a decrease in the spall strength with increasing initial porosity level has been observed experimentally for Ti-6Al-4V alloy (Cui et al., 2022) and aluminum (Yao et al., 2018), and an increase in the spall strength with increasing impact velocity has also been observed experimentally for Ti-6Al-4V alloy (Cui et al., 2022) and aluminum (Yao et al., 2018; Wang et al., 2007). Furthermore, experiments by Cui et al. (2022) showed that a Ti-6Al-4V alloy with 0.29% and 0.88% initial porosity underwent spall fracture when subjected to impact velocities of 500 m/s and 620 m/s, while the same alloy with 5.41% initial porosity only underwent spall fracture at 620 m/s impact velocity.

In our calculations, porosity enters the constitutive relation as a single scalar variable, the void volume fraction. There is no notion of shape, size or spacing of actual discrete voids that exist in real materials. A discrete void in an elastic-viscoplastic matrix, depending on the imposed strain rate and stress state, may collapse into a penny-shape (Nemat-Nasser and Chang, 1990) or fold up and collapse (Swantek and Austin, 2010), both of which will lead to large stress concentrations and can cause early fracture. However, under impact loading conditions similar to those considered here, there is experimental evidence that suggests that discrete voids collapse uniformly without evolving into a shape that induces a large stress concentration (Lovinger et al., 2020; Swantek and Austin, 2010; Lind et al., 2021). Nevertheless, the discreteness of pores may introduce micro-inertia and delay their evolution (Ortiz and Molinari, 1992; Tong and Ravichandran, 1993; Molinari and Mercier, 2001). The stabilizing effect of micro-inertia could also affect the maximum stress level and damage evolution during stress relaxation within the spall plane (Czarnota et al., 2008). Micro-inertia effects are expected to be more important for large discrete voids and for large stress-magnitudes (Sartori et al., 2015; Jacques et al., 2015; Czarnota et al., 2017). Thus, our results that ignore possible micro-inertia effects may be most relevant for materials with a distribution of fine voids that are subject to relatively moderate impact velocities.

The impact loading condition prescribed n our calculations is an imposed velocity for all time, such that $v_L = 0$ for $t > (t_{\mathrm{rise}} + t_{\mathrm{hold}} + t_{\mathrm{decay}})$. This differs from the experimentally imposed impact loading conditions where the impactor generally separates from the target material, eventually leading to a traction free surface. The imposed velocity loading condition, Eq. (5), can result in damage at the impact face for sufficiently large values of v_0 and f_0 for the calculations with stress-controlled porosity nucleation. To confirm that the impact face damage is indeed due to the imposed loading condition, the effects of a finite residual velocity ($v_L > 0$) for $t > (t_{\mathrm{rise}} + t_{\mathrm{hold}} + t_{\mathrm{decay}})$ and of increased decay time, t_{decay}, were investigated with and without including stress-controlled porosity nucleation. These results (not shown here) indicated that imposing a finite value of the residual velocity or increasing the decay time can alleviate the formation of impact face damage. However, neither the dependence of spall fracture on the initial porosity, f_0, or the dependence on impact velocity, v_0, were affected.

6. Conclusions

Finite deformation finite element calculations were carried out to investigate the effects of the initial porosity on the attenuation of the compressive stress wave propagating through the material for a wide range of impact velocities, and to explore the extent to which the attenuation of the compressive stress wave can mitigate porosity-induced spall fracture. Two sets of calculations are carried out, in the first set the material contains initial porosity values ranging from 0% to 5% while in the second set the material also undergoes stress-controlled porosity nucleation. The key conclusions are:

1. The compressive hydrostatic stress pulse leads to plastic deformation and compaction of the porous ductile material, which in turn leads to a decrease in the stress magnitude in the pulse.
2. An increase in initial porosity results in a decrease in the compressive stress magnitude in the initial wave, but decreases the extent of compaction of the porous material.
3. With no stress-controlled porosity nucleation, there is a minimum level of initial porosity below which the remnant porosity level is so low that spall fracture does not occur. There is also a maximum level of initial porosity above which the magnitude of the reflected tensile stress in the pulse is too small for spall fracture to occur.
4. The maximum initial porosity level beyond which the tensile stress magnitude in the reflected pulse is insufficient to cause spall fracture also holds for cases with stress-controlled porosity nucleation.
5. Both with and without stress-controlled porosity nucleation, the maximum level of the initial porosity above which spall fracture does not occur increases with increasing impact velocity.
6. When spall fracture is driven by the evolution of the pre-existing porosity, the spall strength of the material decreases with increasing initial porosity and increases with increasing impact velocity. When spall fracture is driven by stress-controlled porosity nucleation, the spall strength of the material is not very sensitive to the initial porosity level nor to the value of impact velocity, for the range of values considered.

Declaration of competing interest

The authors declare that they have no known competing financial interests or personal relationships that could have appeared to influence the work reported in this paper.

Acknowledgments

This work was supported by the U.S. Department of Energy, National Nuclear Security Administration under Award No. DE-NA0003857. SO and AS also acknowledge the European Union's Horizon 2020 Programme (Excellent Science, Marie-Sklodowska - Curie Actions, H2020-MSCA-RISE-2017) under REA Grant agreement 777896 (Project QUANTIFY). The finite-element calculations were carried out using the high performance research computing resources provided by the Texas A&M University (https://hprc.tamu.edu).

References

Antoun, T., Seaman, L., Curran, D. R., Kanel, G. I., Razorenov, S. V., Utkin, A. V., 2003. Spall fracture. Springer Science & Business Media.

Baumung, K., Bluhm, H., Goel, B., Hoppe, P., Karow, H., Rusch, D., Fortov, V., Kanel, G., Razorenov, S., Utkin, A., et al., 1996. Shock-wave physics experiments with high-power proton beams. Laser and Particle Beams 14 (2), 181–209.

Belytschko, T., Chiapetta, R., Bartel, H., 1976. Efficient large scale non-linear transient analysis by finite elements. International Journal for Numerical Methods in Engineering 10 (3), 579–596.

Boey, C. W., 2009. Investigation of shock wave attenuation in porous materials. Ph.D. thesis, Monterey, California. Naval Postgraduate School.

Bonnan, S., Hereil, P.-L., Collombet, F., Jun. 1998. Experimental characterization of quasi static and shock wave behavior of porous aluminum. Journal of Applied Physics 83 (11), 5741–5749.

Bourne, N., Rosenberg, Z., Johnson, D., Field, J., Timbs, A., Flaxman, R., 1995. Design and construction of the uk plate impact facility. Measurement Science and Technology 6 (10), 1462.

Chen, D., Tan, H., Yu, Y., Wang, H., Xie, S., Liu, G., Yin, Z., 2006. A void coalescence-based spall model. International journal of impact engineering 32 (11), 1752–1767.

Chevrier, P., Klepaczko, J., 1999. Spall fracture: Mechanical and microstructural aspects. Engineering Fracture Mechanics 63 (3), 273–294.

Chu, C., Needleman, A., 1980. Void nucleation effects in biaxially stretched sheets. Journal of Engineering Materials and Technology 102, 249.

Clayton, J., 2005. Modeling dynamic plasticity and spall fracture in high density polycrystalline alloys. International Journal of Solids and Structures 42 (16-17), 4613–4640.

Cortés, R., Jan. 1992. Dynamic growth of microvoids under combined hydrostatic and deviatoric stresses. International Journal of Solids and Structures 29 (13), 1637–1645.

Cortes, R., Elices, M., 1995. Numerical modelling of ductile spall fracture. International journal of impact engineering 16 (2), 237–251.

Cui, Y., Cai, J., Li, Z., Jiao, Z., Hu, L., Hu, J., Mar. 2022. Effect of porosity on dynamic response of additive manufacturing ti-6al-4v alloys. Micromachines 13 (3), 408.

Czarnota, C., Jacques, N., Mercier, S., Molinari, A., 2008. Modelling of dynamic ductile fracture and application to the simulation of plate impact tests on tantalum. Journal of the Mechanics and Physics of Solids 56 (4), 1624–1650.

Czarnota, C., Mercier, S., Molinari, A., 2006. Modelling of nucleation and void growth in dynamic pressure loading, application to spall test on tantalum. International journal of fracture 141 (1-2), 177–194.

Czarnota, C., Molinari, A., Mercier, S., 2017. The structure of steady shock waves in porous metals. Journal of the Mechanics and Physics of Solids 107, 204–228.

Dandekar, D. P., Weisgerber, W. J., 1999. Shock response of a heavy tungsten alloy. International journal of plasticity 15 (12), 1291–1309.

Davis, J.-P., 2020. Thor: a small pulser available to support zfsp materials research. Tech. rep., Sandia National Lab.(SNL-NM), Albuquerque, NM (United States).

Dongare, A. M., Rajendran, A. M., LaMattina, B., Zikry, M. A., Brenner, D. W., 2010. Atomic scale studies of spall behavior in nanocrystalline cu. Journal of Applied Physics 108 (11), 113518.

Erhart, P., Bringa, E. M., Kumar, M., Albe, K., 2005. Atomistic mechanism of shock-induced void collapse in nanoporous metals. Physical Review B 72 (5), 052104.

Flanagan, R. M., Fensin, S. J., Meyers, M. A., Mar. 2022. The role of pre-existing heterogeneities in materials under shock and spall. Applied Physics Reviews 9 (1), 011305.

Gama, B. A., Bogetti, T. A., Fink, B. K., Yu, C.-J., Claar, T. D., Eifert, H. H., Gillespie Jr, J. W., 2001. Aluminum foam integral armor: a new dimension in armor design. Composite structures 52 (3-4), 381–395.

Gurson, A. L., 1977. Continuum theory of ductile rupture by void nucleation and growth: Part 1-yield criteria and flow rules for porous ductile media. Journal of Engineering Materials and Technology 99, 2–15.

Hahn, E. N., Fensin, S. J., Germann, T. C., Gray III, G. T., 2018. Orientation dependent spall strength of tantalum single crystals. Acta Materialia 159, 241–248.

Hashemian, S., Digiacomo, S., Peralta, P., D'Armas, H., Luo, S.-N., Loomis, E., Paisley, D., Byler, D., Dickerson, R., McCllelan, K., 2008. Effects of microstructure on spall damage localization in shock loaded copper multicrystals. In: TMS Annu Meet. Vol. 1. pp. 319–325.

Herrmann, W., May 1969. Constitutive equation for the dynamic compaction of ductile porous materials. Journal of Applied Physics 40 (6), 2490–2499.

Holmes, N., Moriarty, J., Gathers, G., Nellis, W., 1989. The equation of state of platinum to 660 gpa (6.6 mbar). Journal of Applied Physics 66 (7), 2962–2967.

Jacques, N., Mercier, S., Molinari, A., 2015. A constitutive model for porous solids taking into account microscale inertia and progressive void nucleation. Mechanics of materials 80, 311–323.

Jiang, Z., Gao, G., Xiong, X., Wang, Y., 2021. Mechanical response and deformation mechanisms of porous pzt95/5 ceramics under shock-wave compression. Journal of the European Ceramic Society 41 (2), 1251–1262.

Johnson, J. N., 1981. Dynamic fracture and spallation in ductile solids. Journal of Applied Physics 52 (4), 2812–2825.

Jones, D. R., Fensin, S. J., Dippo, O., Beal, R. A., Livescu, V., Martinez, D. T., Trujillo, C. P., Florando, J., Kumar, M., Gray III, G. T., 2016. Spall fracture in additive manufactured ti-6al-4v. Journal of Applied Physics 120 (13), 135902.

Jones, D. R., Fensin, S. J., Ndefru, B. G., Martinez, D. T., Trujillo, C. P., Gray, G. T., Dec. 2018. Spall fracture in additive manufactured tantalum. Journal of Applied Physics 124 (22), 225902.

Jones, D. R., Morrow, B. M., Hollis, K. J., 2020. Gas gun flyer plate impact testing of stainless steel deposited by low pressure plasma spraying and cold gas dynamic spraying. Journal of Thermal Spray Technology 29 (4).

Kanel, G., 2010. Spall fracture: methodological aspects, mechanisms and governing factors. International journal of fracture 163 (1), 173–191.

Koller, D., Hixson, R., Gray III, G., Rigg, P., Addessio, L., Cerreta, E., Maestas, J., Yablinsky, C., 2005. Influence of shock-wave profile shape on dynamically induced damage in high-purity copper. Journal of applied physics 98 (10), 103518.

Kraus, R. G., Chapman, D. J., Proud, W. G., Swift, D. C., Jun. 2009. Hugoniot and spall strength measurements of porous aluminum. Journal of Applied Physics 105 (11), 114914.

Laurençon, M., de Rességuier, T., Loison, D., Baillargeat, J., 2020. Dynamic behaviour and spall fracture of laser shock-loaded AlSi10Mg alloy obtained by selective laser melting. In: Lane J.M.D., Germann T.C., Armstrong M.R., Wixom R., Damm D., Zaug J. (Eds.), AIP Conf. Proc. Vol. 2272. American Institute of Physics Inc.

Li, J., Xu, X., Duan, Y., Ren, H., 2019. Fracture mechanism of steel plate loaded by explosive-induced shock waves. Engineering Failure Analysis 101, 243–256.

Lind, J., Nelms, M. D., Robinson, A. K., Kumar, M., Barton, N. R., 2021. Examining material constitutive response under dynamic compression and large plastic strains using in situ imaging of hole closure. Acta Materialia 206, 116584.

Liu, Y., Zheng, X., Osovski, S., Srivastava, A., 2019. On the micromechanism of inclusion driven ductile fracture and its implications on fracture toughness. Journal of the Mechanics and Physics of Solids 130, 21–34.

Lovinger, Z., Czarnota, C., Ravindran, S., Kettenbeil, C., Molinari, A., Ravichandran, G., 2020. Shock structure and spall behavior of porous aluminum. In: AIP Conference Proceedings. Vol. 2272. AIP Publishing LLC, p. 120015.

Mallick, D., Parker, J., Wilkerson, J., Ramesh, K., 2020. Estimating void nucleation statistics in laser-driven spall. Journal of Dynamic Behavior of Materials 6 (3), 268–277.

Me-Bar, Y., Boas, M., Rosenberg, Z., 1987. Spall studies on ti-6al-4v. Materials Science and Engineering 85, 77–84.

Molinari, A., Mercier, S., 2001. Micromechanical modelling of porous materials under dynamic loading. Journal of the Mechanics and Physics of Solids 49 (7), 1497–1516.

Moore, J. A., Li, S. F., Rhee, M., Barton, N. R., Dec. 2018. Modeling the Effects of Grain and Porosity Structure on Copper Spall Response. Journal of Dynamic Behavior of Materials 4 (4), 464–480.

Nemat-Nasser, S., Chang, S.-N., 1990. Compression-induced high strain rate void collapse, tensile cracking, and recrystallization in ductile single and polycrystals. Mechanics of Materials 10 (1-2), 1–17.

Nemat-Nasser, S., Hori, M., 1987. Void collapse and void growth in crystalline solids. Journal of applied physics 62 (7), 2746–2757.

N'souglo, K. E., Srivastava, A., Osovski, S., Rodríguez-Martínez, J. A., 2018. Random distributions of initial porosity trigger regular necking patterns at high strain rates. Proceedings of the Royal Society A: Mathematical, Physical and Engineering Sciences 474 (2211), 20170575.

Ortiz, M., Molinari, A., 1992. Effect of strain hardening and rate sensitivity on the dynamic growth of a void in a plastic material.

Osovski, S., Srivastava, A., Ponson, L., Bouchaud, E., Tvergaard, V., Ravi-Chandar, K., Needleman, A., 2015. The effect of loading rate on ductile fracture toughness and fracture surface roughness. Journal of the Mechanics and Physics of Solids 76, 20–46.

Pan, J., Saje, M., Needleman, A., 1983. Localization of deformation in rate sensitive porous plastic solids. International Journal of Fracture 21 (4), 261–278.

Peirce, D., Shih, C. F., Needleman, A., 1984. A tangent modulus method for rate dependent solids. Computers & structures 18 (5), 875–887.

Pramod, B., Raj, J. P., Parashar, C., Kartha, A., Nagaraja, S., 2019. Attenuation of shock waves by using porous media. In: AIP Conference Proceedings. Vol. 2080. AIP Publishing LLC, p. 030015.

Reinhart, W. D., Chhabildas, L. C., Carroll, D. E., Bergstresser, T. K., Thornhill, T. F., Winfree, N. A., 2001. Equation of state measurements of materials using a three-stage gun to impact velocities of 11 km/s. International journal of impact engineering 26 (1-10), 625–637.

Remington, T., Hahn, E., Zhao, S., Flanagan, R., Mertens, J., Sabbaghianrad, S., Langdon, T. G., Wehrenberg, C., Maddox, B., Swift, D., et al., 2018. Spall strength dependence on grain size and strain rate in tantalum. Acta Materialia 158, 313–329.

Rybakov, A., 2001. Experimental study of spall-fracture zone. International journal of solids and structures 38 (30-31), 5453–5464.

Sartori, C., Mercier, S., Jacques, N., Molinari, A., 2015. Constitutive behavior of porous ductile materials accounting for micro-inertia and void shape. Mechanics of Materials 80, 324–339.

Srivastava, A., Osovski, S., Needleman, A., 2017. Engineering the crack path by controlling the microstructure. Journal of the Mechanics and Physics of Solids 100, 1–20.

Srivastava, A., Ponson, L., Osovski, S., Bouchaud, E., Tvergaard, V., Needleman, A., 2014. Effect of inclusion density on ductile fracture toughness and roughness. Journal of the Mechanics and Physics of

Solids 63, 62–79.
Swantek, A., Austin, J., 2010. Collapse of void arrays under stress wave loading. Journal of Fluid Mechanics 649, 399–427.
Tang, J., Xiao, J., Deng, L., Li, W., Zhang, X., Wang, L., Xiao, S., Deng, H., Hu, W., 2018. Shock wave propagation, plasticity, and void collapse in open-cell nanoporous ta. Physical Chemistry Chemical Physics 20 (44), 28039–28048.
Thissell, W. R., Zurek, A. K., Tonks, D. L., Hixson, R. S., 2000. Experimental quantitative damage measurements and void growth model predictions in the spallation of tantalum. In: AIP Conference Proceedings. Vol. 505. American Institute of Physics, pp. 451–454.
Thomason, P., 1999. Ductile spallation fracture and the mechanics of void growth and coalescence under shock-loading conditions. Acta materialia 47 (13), 3633–3646.
Tong, W., Ravichandran, G., 1993. Dynamic pore collapse in viscoplastic materials. Journal of applied physics 74 (4), 2425–2435.
Tong, W., Ravichandran, G., 1995. Inertial effects on void growth in porous viscoplastic materials. Journal of Applied Mechanics 62 (3), 633.
Trunin, R., Medvedev, A., Funtikov, A., Podurets, M., Simakov, G., Sevast'yanov, A., 1989. Shock compression of porous iron, copper and tungsten: and their equation of state in the terapascal pressure range. Sov. Phys. JETP 68 (2), 356–361.
Turley, W., Fensin, S. J., Hixson, R., Jones, D. R., La Lone, B., Stevens, G., Thomas, S., Veeser, L. R., 2018. Spall response of single-crystal copper. Journal of Applied Physics 123 (5), 055102.
Tvergaard, V., 1981. Influence of voids on shear band instabilities under plane strain conditions. International Journal of fracture 17 (4), 389–407.
Tvergaard, V., 1982a. Influence of void nucleation on ductile shear fracture at a free surface. Journal of the Mechanics and Physics of Solids 30 (6), 399–425.
Tvergaard, V., 1982b. On localization in ductile materials containing spherical voids. International Journal of fracture 18 (4), 237–252.
Tvergaard, V., Needleman, A., 1984. Analysis of the cup-cone fracture in a round tensile bar. Acta metallurgica 32 (1), 157–169.
Tvergaard, V., Needleman, A., 1992. Effect of crack meandering on dynamic, ductile fracture. Journal of the Mechanics and Physics of Solids 40 (2), 447–471.
Walsh, J. M., Christian, R. H., 1955. Equation of state of metals from shock wave measurements. Physical review 97 (6), 1544.
Wang, Y., He, H., Qi, M., Shen, L., Bai, B., 2007. Time-resolved dynamic compaction and tensile fracture of low-porosity aluminum under impact loading. Journal of Applied Physics 102 (7), 073518.
Wang, Y., Qi, M., He, H., Wang, L., 2014. Spall failure of aluminum materials with different microstructures. Mechanics of Materials 69 (1), 270–279.
Wright, T., Ramesh, K., 2008. Dynamic void nucleation and growth in solids: a self-consistent statistical theory. Journal of the Mechanics and Physics of Solids 56 (2), 336–359.
Xu, A., Zhang, G., Li, H., Ying, Y., Zhu, J., 2011. Dynamical similarity in shock wave response of porous material: From the view of pressure. Computers & Mathematics with Applications 61 (12), 3618–3627.
Yao, Y., Chai, H., Li, C., Bie, B., Xiao, X., Huang, J., Qi, M., Luo, S., 2018. Deformation and damage of sintered low-porosity aluminum under planar impact: Microstructures and mechanisms. Journal of Materials Science 53 (6), 4582–4597.